ELSEVIER

Remote Sensing of Environment 76 (2001) 373–385

Remote Sensing of Environment

www.elsevier.com/locate/rse

Uncertainty propagation in models driven by remotely sensed data

Michele Crosetto[a], José Andrés Moreno Ruiz[b], Bruno Crippa[c,*]

[a]European Commission, Joint Research Centre, Global Vegetation Monitoring Unit, Space Applications Institute, 21020 Ispra (Va), Italy
[b]Departamento de Lenguajes y Computación, Universidad de Almería, 04120 Almería, Spain
[c]Dipartimento di Rappresentazione e Progetto, Università di Messina, 98166 Messina, Italy

Received 28 July 2000; accepted 18 December 2000

Abstract

Often, little importance is given to the problem of how uncertainty propagates in models driven by remotely sensed data, and what the effects of uncertainty might be on the output of these models. In this paper, a general procedure to support a characterisation of uncertainty in the generation of remote sensing (RS) products is proposed. The procedure can be used with models characterised by any degree of complexity and driven by any kind of data. It provides two useful tools to analyse models: uncertainty analysis (UA), which allows the assessment of the uncertainty associated with model output, and sensitivity analysis (SA), which is useful to determine how much each source of uncertainty contributes to model output uncertainty. Uncertainty modelling, i.e. finding suitable tools to represent uncertainty, is a key step in performing UA and SA. A general error model for quantitative raster data is described. Different applications of UA and SA are proposed, and, in the last part of the paper, an example of UA and SA on a model for burned area detection is discussed.

1. Introduction

The international scientific community recognises remote sensing (RS) systems as important sources of data for global change research. In order to derive high-level products suitable to support this research, raw RS data must undergo a sequence of processing and analysis stages. In this paper, the term model is used to indicate a chain of computational procedures and algorithms suitable to derive high-level products (model output) from raw RS data (model input).

Besides providing data for scientific research, RS products can support the decision process in environmental management, e.g. through the monitoring of natural hazards. These two important applications represent a challenge for the RS community, because they require a complete quantitative characterisation of the quality of the generated products.

Looking at the entire range of techniques used in geomatics, sound procedures to evaluate the quality of the generated products are available in geodesy (Moritz, 1980), surveying, and photogrammetry (Mikhail, 1976). There, the models that tie input data and outputs consist of analytical, continuously differentiable functions. An example is given by a photogrammetric network that tie the image coordinates and the coordinates of cartographic features. Coupling these models with suitable stochastic models of the observations, it is possible to provide an estimate of the model output and the associated precision. Furthermore, working as usual with data redundancy (i.e. the number of observations is larger than the number of model outputs), suitable procedures can make these techniques statistically robust against outliers in input data (Granshaw, 1980). Hence, they can guarantee very high quality standards.

Similar standards can be provided by RS techniques based on geometric models, like optical stereoscopy and SAR interferometry for digital elevation model generation. The same applies to RS techniques based on the inversion of models that derive directly from the laws of physics and describe the radiation transfer through the atmosphere and its scattering at the surface. Examples of physically based models can be found in Pinty, Verstraete, and Dickinson (1990) and Rahman, Pinty, and Verstraete (1993).

The same cannot be said for most RS techniques. The reason is manyfold. First, these techniques make use of models that consist of complex algorithm chains rather than

* Corresponding author. DIIAR, Sezione Rilevamento, Politecnico di Milano, 20133 Milano, Italy. Tel.: +39-02-2399-6503; fax: +39-02-2399-6530.

E-mail address: bruno@ipmtf4.topo.polimi.it (B. Crippa).

0034-4257/01/$ – see front matter
PII: S0034-4257(01)00184-5

analytical functions. Therefore, output precision cannot usually be expressed in an analytical form. Dealing with thematic aspects, like vegetation classes and change detection, is complicated, because problems arise even in finding a precise definition of what actually is the model output. Taking vegetation maps, for example, a precise definition of vegetation classes, minimum mapping unit areas, etc. is sometimes lacking in the RS products. Additional problems are encountered by RS applications focused on 3D phenomena, e.g. the monitoring of active fires. In fact, moving from 2D to 3D increases the difficulty in characterising product quality.

Consequently, for a large number of RS applications, the deterministic approach seems to be the most widely adopted. Once a suitable model has been chosen and the corresponding inputs have been collected, model and input data are implicitly treated as without uncertainty and the model output is calculated in a deterministic way. A limited assessment of output quality is sometimes derived by validation, against ground truth, on small portions of the output. However, the validation becomes very critical when RS products cover a wide space–time domain. An example is given by weekly global coverage maps spanning a decade. It follows that the uncertainty associated with RS products is either roughly evaluated or disregarded.

In this paper, a general procedure to support a characterisation of uncertainty in the generation of RS products is proposed. The procedure can be used with models characterised by any degree of complexity and driven by any kind of data. It provides two useful modelling tools: uncertainty analysis (UA) and sensitivity analysis (SA). UA allows the assessment of the uncertainty associated with RS model output as a result of propagation through the model of uncertainty in input data and model parameters. SA is useful to determine how much each individual source of uncertainty contributes to the model output uncertainty. Different synonyms for UA and SA can be encountered in the literature. The above definitions refer to the convention employed in Saltelli, Chan, and Scott (2000), a handbook of SA, which encompasses a wide range of modelling applications.

In this paper, emphasis is given to both the description of UA and the discussion of a general approach suitable to represent uncertainty in RS applications, while the SA is only briefly outlined. More details can be found in Crosetto and Tarantola (2000). The paper begins with a discussion of UA. This is followed by sections discussing SA, the synergetic use of UA and SA, and error modelling. Section 6 describes an example of UA and SA on a model for burned area detection based on the NOAA/NASA Pathfinder AVHRR 8 km Land Data Set (James & Kalluri, 1994). Conclusions follow.

2. Uncertainty analysis

The goal of UA is to assess the uncertainty associated with the output of the model at hand. In the literature, UA is often referred to as uncertainty propagation or error propagation (Heuvelink, 1998). The problem can be formulated as follows. The model represents the relationship between the input data I_i, with $i = 1, \ldots, K$ and the output Y, and can be described by

$$Y = f(p_1, p_2, \ldots, p_M, I_1, I_2, \ldots, I_K) \quad (1)$$

where the operator $f(\cdot)$ is a chain of computational procedures and algorithms. The model incorporates a set of model parameters p_i, with $j = 1, \ldots, M$. The operator $f(\cdot)$ maps the space of the input data and model parameters to that of the output variable Y. In the following, Y is considered a scalar variable. Since in RS applications it often happens that Y is a 2D or 3D field of values, a suitable summary variable needs to be identified. The identification of a summary value is common practice in science-based decision making, whereby decision makers need to understand the problem in a compact, though exhaustive, way. For instance, if the RS output consists of a series of burnt area maps, a possible summary value could be the total burned area in a given period.

It is important to note that the UA is solely concerned with the uncertainty associated with Y due to propagation through $f(\cdot)$ of input data errors and uncertainty in model parameters. Examples of model parameters p_j are the coefficients of a multiple regression or the threshold values of a given RS algorithm. UA assumes that an appropriate model $f(\cdot)$ has been selected (i.e. that bias is negligible). Since p_j's are a part of the model itself, it is implicitly assumed that unbiased estimates of p_j's are available. However, an unbiased procedure can only provide estimates with a given level of precision, that is to say with a given estimate dispersion. The effect of the uncertainty associated with p_j is studied in the UA.

UA involves three main steps: the identification of all sources of uncertainty in input data I_i and model parameters p_j; uncertainty modelling; and uncertainty propagation. Uncertainty modelling, i.e. finding appropriate tools to represent uncertainty, is discussed in detail in Section 5.

Different analytical and numerical techniques to perform uncertainty propagation have been proposed (Heuvelink, 1998). Analytical techniques can usually be applied under particular conditions on the operator $f(\cdot)$. For instance, the method based on the law of variance propagation, employed in many fields of geomatics, can be only used when $f(\cdot)$ is a continuously differentiable function. This condition is often not satisfied by RS models. Despite this limitation, the method offers the advantage of yielding the analytical expression of the variance of Y. Numerical techniques do not yield results in analytical forms, but usually pose less strict conditions on $f(\cdot)$.

For the sake of generality, a numerical method for error propagation (Monte Carlo (MC) method) is described in the following section. Since it treats $f(\cdot)$ as a black box, it represents a flexible tool for UA, which is generally applicable in the field of RS models.

2.1. The MC method

The MC method allows UA to be performed without requiring assumptions upon the model structure. In a first step, all input data and model parameters affected by uncertainty that can affect the uncertainty of Y must be identified. Then, a suitable way to quantify and describe uncertainty is needed (error modelling). An error model is a stochastic model capable of generating a population of error-corrupted versions of the same reality, in this context I_i or p_j (Goodchild, Guoqing & Shiren, 1992). Each error-corrupted version, also named realisation, is a sample from the same population and differences between realisations represent the uncertainty present in I_i or p_j. In case of a scalar variable, like the temperature at a given location, a suitable error model can be based on a normal distribution, whose variance represents the measurement uncertainty.

The term input factor is used to indicate a random variable associated with a given I_i (p_j) affected by uncertainty in order to drive the generation of error-corrupted versions of I_i (p_j) in the MC simulation. In case of a scalar variable, the corresponding input factor represents the error associated with this variable. As it is described in Section 5, the uncertainty of more complex type of input data, e.g. fields of attribute data, can be decomposed in different components. It is possible to treat these components separately using suitable models. In such cases, the generation of error-corrupted versions of a single input can be driven by a set of input factors, with each factor representing a particular aspect of uncertainty. For the purpose of UA and SA, the model can be written as:

$$Y = f(X_1, X_2, \ldots, X_K)$$

where the X_k's, with $k = 1, \ldots, K$, are the input factors that are meant to capture all sources of uncertainty. It must be noted that nominal values will be used in the model for all I_i and p_j whose uncertainty can be disregarded.

The idea of the MC method is then to calculate outputs from model (1) repeatedly, with error-corrupted versions of I_i and p_j. The method involves the following steps:

(1) Repeat N times (N_{MC}):
- Generate randomly a set of realisations of the input factors X_k, with $k = 1, \ldots, K$; the set of realisations, called a sample, is used to generate the corresponding realisations of the associated I_i and p_j.
- Evaluate the model, i.e. use the realisations of I_i and p_j in model (1) and compute the corresponding Y.

(2) Compute statistics from the set of Y^i, with $i = 1, \ldots, N_{MC}$, which represents an empirical probability density function (PDF) of Y. The main characteristics of the PDF, like the sample variance and higher-order moments, can be estimated, giving a full characterisation of the stochastic features of Y with an arbitrary level of precision, which is related to the number of samples N_{MC} (Heuvelink, 1998).

In this specific context, the term precision refers to the dispersion of the estimates of the PDF features. A measure of the dispersion is the variance. The larger N_{MC}, the less dispersed the estimates are. However, the same cannot be said about the accuracy of these estimates, that is the extent to which the estimates approach the true values of the PDF features. The accuracy is conditional on the quality of the stochastic models associated with I_i and p_j. These models describe the uncertainty associated with input data and model parameters. Their quality can be only checked by employing external information. The same applies to the other UA techniques. In other words, for a stochastic approach to RS, beside the model $f(\cdot)$ validation, which is usually performed, an additional validation (the validation of the stochastic model) is required.

The overall computational cost of the MC procedure depends basically on the cost of the model evaluation. Depending on model complexity, the numerical load of performing N_{MC} model evaluations can be high. This is the main disadvantage of the procedure, while the most important advantages are the ease of implementation and the ability to evaluate models characterised by any degree of complexity.

3. Sensitivity analysis

UA is focused on how uncertainty in input data and model parameters propagates through the model and affects the model output. SA considers uncertainty in the opposite direction (from the output back to the input) determining how much each individual source of uncertainty contributes to the output uncertainty. UA and SA cover complementary aspects. Their synergetic use can support important applications related to RS models (see the next section). Many techniques for SA are described in the literature. A thorough description of SA techniques can be found in Saltelli et al. (2000).

In the following, the basic concepts of a particular kind of SA technique, developed at the Institute for Systems, Informatics, and Safety of the Joint Research Centre and used by the authors in the case study described in Section 6, are outlined. This technique, named extended FAST (Saltelli, Tarantola & Chan, 1999), is an advanced version of the Fourier Amplitude Sensitivity Test (FAST) proposed by Cukier, Fortuin, Schuler, Petschek and Schaibly (1973). Both FAST and extended FAST are variance-based techniques that employ MC simulation performed with a particular sampling strategy. These techniques assume the input factors X_i to be independent and allow the sensitivity indices to be calculated. It must be noted that the hypothesis of independence does not concern I_i and p_j.

For a given input factor X_i, the sensitivity index represents the fractional contribution to the variance of the model output Y, which is due to X_i. In order to calculate the sensitivity indices, the total variance V of Y is apportioned to all the input factors X_i as:

$$V = \sum_i V_i + \sum_{i<j} V_{ij} + \sum_{i<j<m} V_{ijm} + \ \ldots \ + V_{12 \ \ldots \ k}$$

where

$$V_i = V[E(Y|\ X_i = x_i^*)]$$

$$V_{ij} = V[E(Y|\ X_i = x_i^*,\ X_j = x_j^*)] - V[E(Y|\ X_i = x_i^*)] - V[E(Y|\ X_j = x_j^*)]$$

and so on. $E(Y|\ X_i{=}x_i^*)$ denotes the expectation of Y conditional on X_i having a fixed value x_i^*, and the operator $V[\cdot]$ denotes the conditional variance. The first-order sensitivity index S_i for the factor X_i is defined as:

$$S_i = \frac{V_i}{V}. \tag{2}$$

The reason is intuitive: If the conditional mean $E(Y|X_i{=}x_i^*)$ varies considerably with the value x_i^* for X_i, while all the effects of the X_j's, $j \neq i$ are being averaged, then surely, factor X_i is an influential one. As already mentioned above, the sensitivity indices are estimated using MC simulation and a particular sampling design, e.g. the FAST (Cukier et al., 1973) and the method of Sobol' (1993).

Formula (2) refers to the first-order indices. Higher-order sensitivity indices, responsible for interaction effects among input factors, are usually not estimated. The extended FAST provides, for each X_i, estimates of the S_i and of the total sensitivity indices S_{Ti}, defined as the sum of all the indices (S_i and higher orders) where X_i is included, thus, concentrating in one single term all the interactions involving X_i. The estimation of S_i and S_{Ti} is important to appreciate the difference between the impact of factor X_i alone on Y, measured by S_i and the overall impact of factor X_i through interactions with the others on the Y, measured by S_{Ti}.

Advantages of the extended FAST are the model independence and the ability to capture interaction effects. A limitation is related to its computational load. For a general discussion, see Crosetto & Tarantola (2000) and Saltelli et al. (1999). Useful information can be also found at http://sensitivity-analysis.jrc.cec.eu.int/.

4. Synergetic use of uncertainty and sensitivity analyses

UA and SA can be employed as effective tools in both RS modelling and in the use of existing RS models. Some possible applications are briefly described.

(1) In the building stage of a new RS model, UA and SA can be used to identify influential sources of uncertainty, giving important hints to the modeller. For instance, if the uncertainty associated with an input has a strong influence on the model output, the attention of the modeller has to be focused on this input in order to reduce the influence of its uncertainty. The same applies to the uncertainty associated with model parameters. To illustrate this application, an example of analysis of a burnt area detection algorithm is described in Section 6.

(2) During the stage of building a new RS model, it can be useful to consider the quality of the model itself. This is important because a given RS task can often be accomplished using two or more alternative models. These models can use different approximations, require different computational costs, and achieve different levels of accuracy. UA and SA can be used as a tool to choose, out of a group of alternative models suitable for a given application, the best one in term of cost–benefit analysis (Crosetto and Tarantola, 2000). This can be obtained by treating the subjective decision of the modeller (e.g. model X vs. model Y) as an input factor, and analysing its impact on the model output.

(3) In the implementation of new expensive models driven by RS data and other types of data, UA and SA can be used to find an optimal allocation of resources for input data acquisition that allows the achievement of a given precision in the model output. This can be done employing a low-cost strategy, based on simulations on a small prototype of the entire model. The precision is analysed through UA, and the maximum benefit at minimum cost is obtained through SA by focusing resources on the acquisition of the subset of input data with the highest impact on the output variance.

5. Error modelling

Error modelling is a key step in performing UA and SA. An appropriate error model must be associated with each input and model parameter affected by uncertainty. Fields of quantitative attribute data, also called quantitative raster data, represent the most common input type in RS models. RS models are usually not driven by categorical attribute data. A general model for quantitative raster data and a rigorous procedure to characterise the main parameters of the model are described in Sections 5.1. and 5.2. The modelling of a particular aspect of uncertainty associated with RS images, the mask effect due to cloud cover, is then addressed. A short review of error models for different types of spatial data can be found in (Crosetto and Tarantola, 2000).

5.1. An error model for quantitative raster data

Quantitative raster data are fields of quantitative spatial attributes A. RS images are 2D fields of quantitative attributes. However, when a time series of images is fed into a model, it is convenient to treat the series as a 3D

field, and to associate with this field an appropriate 3D error model. The attribute A in RS images can consist of a single value or a vector of values for each pixel. These two cases correspond to single channel and multichannel images, respectively. In the following, the first case is considered. When a quantitative field A is one of the inputs of a RS model, usually, only a particular realisation S of this field is available. A general error model for this kind of data can be introduced:

$$Z(\bar{x}) \equiv S(\bar{x}) + N(\bar{x}) \quad (3)$$

where S is the deterministic field, Z the corresponding error-corrupted random field, N the error random field with mean $m_N = E[N(\bar{x})]$ and variance $\sigma_N{}^2$, and $\bar{x}$ represents the domain of the functions Z, S, and N. A random field is also called a stochastic process. This model represents two important features of uncertainty: a systematic attribute error, or bias, is introduced by fixing nonzero mean values m_N; a stochastic attribute error is introduced by setting N to be random with variance–covariance matrix C_{NN}. In case of a 2D field, with l rows and m columns, C_{NN} is a $l \times m$ by $l \times m$ matrix, which enables representation of the spatial correlation of N. If the error field N has no spatial correlation, the variance matrix takes the form:

$$C_{NN} = \sigma_N^2 \cdot I$$

where I is the identity matrix and the variance $\sigma_N{}^2$ represents the dispersion of the random error. A spatially uncorrelated error is also called a white noise. In the more general case, nonzero values in the off-diagonal elements of C_{NN} describe, and, hence, allow simulation of the spatial correlation structure of N.

A procedure to evaluate the main features of N and to generate randomly its realisations is described in the following section.

5.2. A procedure to characterise and simulate error fields

In order to use the above error model in MC simulation, suitable techniques to characterise the features of the random field N and efficient ways to generate realisations of N, and, hence, of Z, have to be employed. The characterisation of the features of N is a key step in the procedure, which requires the exploitation of all the available information about the stochastic properties of input data (data measurement techniques, expert opinion, etc.). The first part of this section describes a procedure to estimate the main characteristics of the C_{NN}. The second part illustrates a rigorous method to generate realisations of N. In the following, 2D fields are considered.

Let us assume that a realisation M of the error random field N is available. This can be obtained by comparing the values of the observed image S against some reference values measured with a more precise and independent procedure. When reference values are not available, some information on N can be derived by comparing at least two observations, i.e. two images, of the same target. If the target variations between the two observations are negligible and the acquisition geometry of the two images is similar, the image obtained by differencing the two observed images can be used to derive estimates of N. For instance, if the error that affects the values in corresponding pixels of the observed images can be considered independent, an estimate of σ_N^2 is given by $\sigma_N^2 = \sigma_{DI}^2/2$, where σ_{DI}^2 is the variance of the difference image.

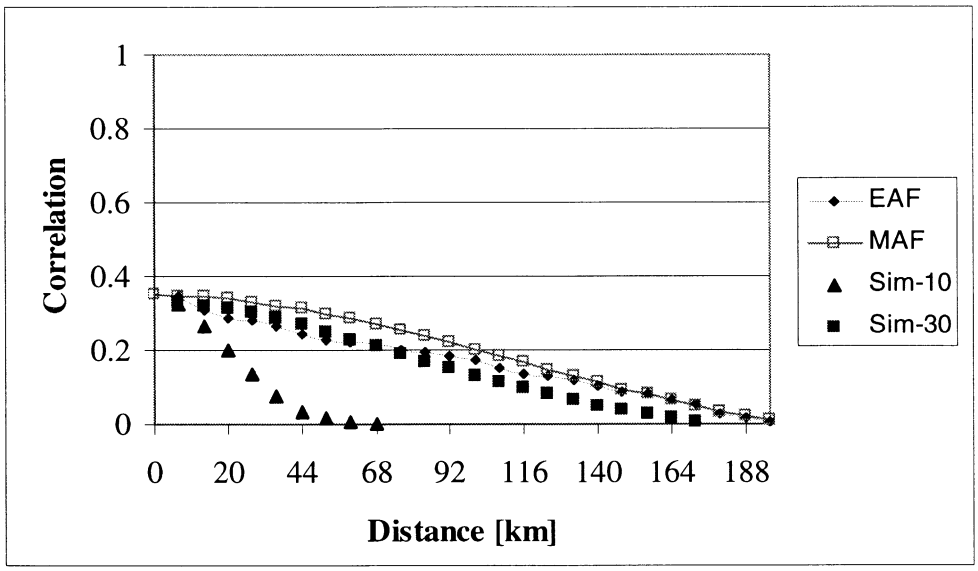

Fig. 1. EAF and MAF calculated on the difference image of two 50×50 pixel AVHRR Ch1 images of the Saharan desert. The EAFs of two simulated realisations (Sim-10, with a 10-pixel band $\mathbf{C}_{NN}$, and Sim-30, with a 30-pixel band) are also reported.

Given a realisation M of N, with the assumption that N is a homogeneous and isotropic stochastic process, C_{NN} can be estimated using a procedure extensively employed in geodesy in the collocation technique with least squares (Knudsen, 1987; Moritz, 1980; Sansò, 1986). Alternative procedures may be based on the variogram (Heuvelink, 1998). The first step consists of calculating the so-called empirical autocovariance function (EAF) $C(d_K)$, whose values are second-order statistics:

$$C(d_K) = \frac{1}{n_T} \times \sum_{i=1}^{n_T} \left\{ [M(P_i) - m_M] \frac{1}{n_j} \sum_{j=1}^{n_j} [M(P_j) - m_M] \right\} \quad (4)$$

where $d_K = K\Delta$ is the distance from the origin, Δ the step of the function, $n_T = lm$ the total image pixel number, $M(P_i)$ the image value in the pixel P_i, m_M the mean image value, and n_j the total number of pixels P_j that, for a given P_i, satisfy the condition: $(K-1)\Delta < |P_i - P_j| < K\Delta$.

The empirical values must be interpolated with suitable positive definite functions (obtaining the model autocovariance function, MAF) to ensure the nonsingularity of the variance–covariance matrix $\mathbf{C}_{NN}$ (Barzaghi & Crippa, 1990). An example of MAF of an error field is depicted in Fig. 1. The MAF values, normalised by dividing by σ_N^2, indicate the spatial correlation of the error field. From this function, the following information can be derive:

1. $\sigma^2_{N\_Corr}$, the variance of the correlated part of the error field, is given by the intersection of the MAF with the correlation axis, 34% of σ_N^2 in the example.
2. $\sigma^2_{N\_\mathbf{W}}$, the variance of the noncorrelated part of the error field, is given by the difference $\sigma^2_{N\_\mathbf{W}} = \sigma_N^2 - \sigma^2_{N\_Corr}$.
3. The correlation extent is measured by the correlation length L, i.e. the distance from the origin where the MAF has a correlation that is half of that in the origin.

Using the MAF, it is straightforward to build the C_{NN}. The MAF can slowly approach zero, indicating that a correlation exists between the error in very distant pixels of the image. Finite autocovariance functions can be used, which have zero correlation after a specified distance. This approximation results in a band matrix structure of the C_{NN}, which allows memory requirements of C_{NN} and processing time for the simulation to be reduced. Suitable techniques can be used to process such matrices. The results described in this work were obtained by treating C_{NN} as a band matrix.

Once the C_{NN} has been built, the simulation of a realisation N' from N can be obtained by multiplying the lower triangular matrix L of the Cholesky decomposition of C_{NN}, by a matrix W of normally distributed white noise, with $\sigma^2_{\mathbf{W}} = 1$:

$$N' = \mathrm{L} \cdot \mathrm{W}.$$

Therefore, the generation of realisations N' is obtained through the following steps:

1. Build the band matrix C_{NN}, calculate the Cholesky decomposition, and store L. Note that, as C_{NN} is a band matrix, L is also a band matrix. This is the more computationally expensive step, which is only performed once.
2. For each MC run, randomly generate the normally distributed white noise W and calculate $N' = L \cdot W$.

The characteristics of the simulated N' can be controlled by calculating its EAF. In Fig. 1, the EAFs of two different realisations N' (the first one obtained with a 10-pixel band C_{NN}, and the other one with a 30-pixel band) can be compared with the originally estimated EAF and MAF of N. One may notice that the larger the employed band, the better the structure of N' approximates that of N.

It is important to discuss how to choose the input factors using the above error model. The systematic and stochastic components of the error are described by different types of parameters. The systematic error affects all the $l \times m$ pixels of the given 2D field in the same way. In the UA and SA, it can be treated as a simple scalar variable. The same cannot be done for the stochastic error because, assuming, for instance, $C_{NN} = \sigma_N^2 \cdot \mathrm{I}$, a single parameter σ_N^2 controls the generation of $l \times m$ different values. This poses problems in the SA, i.e. in the output variance decomposition. As it is described in Crosetto and Tarantola (2000), an empirical way to treat this kind of parameter is to use a random switch between two configurations as input factor: In the first one, the stochastic error is generated and added to the 2D field, while in the second one, no stochastic error is added. With this stratagem, the sensitivity index associated with such an input factor measures how sensitive the model output is to the switch, and, hence, it gives an indication of how sensitive it is to the stochastic error.

In the following section, a slightly different use of the above-described procedure is proposed, in order to take into account a particular type of uncertainty in RS data: the "mask effect" on the images due to cloud cover. The readers not directly interested in this fairly specific topic are referred to the case study described in Section 6.

5.3. Modelling the mask effect due to cloud cover on raster data

It is known that the quality of optical and thermal RS images is strongly affected by cloud cover. Clouds can either completely mask the signal or degrade its information content (e.g. in case of partially covered pixels). The fact that pixels of RS images can be masked or corrupted by clouds can be seen

as a particular type of uncertainty in RS model inputs. In the following, a procedure to model this effect is described.

In order to consider the mask effect as a separate component of uncertainty in quantitative raster data, model (3) can be written as:

$$Z(\bar{x}) \equiv S(\bar{x}) + N(\bar{x}); \quad \mathrm{M}(\bar{x})$$

where $\mathrm{M}(\bar{x}) \equiv \mathrm{M(i,j)}$ is a $l \times m$ binary mask image that affects the values z_{ij} of $Z(\bar{x}) \equiv Z(i,j)$ in this way:

$$Z(i,j) = z_{ij} \quad \text{if } M(i,j) = 0$$

$$Z(i,j) = \mathrm{NaN} \quad \text{if } M(i,j) = 1$$

NaN means that the pixel is masked. With this model, three separate components of uncertainty can be represented: systematic error, stochastic error and the uncertainty due to mask effect. Employing in the SA three input factors, it is possible to evaluate the individual contribution of each component to the output uncertainty.

The mask matrix M> has to be randomly generated N times in the MC simulation. The main characteristic of M is the proportion P of mask pixels. Disregarding the spatial aggregation of the masks, for each MC run, M can be generated by repeating the following $l \times$ M times:

- for pixel (i,j), generate e from a uniform distribution $U[0,1]$;
- set $\mathrm{M(i,j)} = 1$ if $e \leq P$, and $\mathrm{M(i,j)} = 0$ otherwise.

Mask effects are often characterised by some spatial aggregation. Hence, it is important to address this aspect in the modelling. It must be noted, however, that the required accuracy in modelling a given component of uncertainty is very dependent on the analysed RS model. Some models can be totally insensitive to spatial aggregation of masks.

A modified version of the procedure described in the previous section can be employed to characterise the level of mask aggregation and to simulate mask images. In the following, it is assumed that at least a mask image R is available. This image could be the output of a cloud detection algorithm used on a representative image.

The proportion of mask pixels P can be evaluated directly on R. A second parameter, related to the level of mask aggregation, can be obtained computing the EAF of R. This can be done using formula (4) and substituting M with R. From the EAF, the correlation length L_R can be chosen as a suitable indicator of the level of mask aggregation. The example reported in Fig. 2 illustrates the EAFs computed for four different synthetic masks. One may notice that the correlation length is proportionally dependent on the level of mask aggregation.

The generation of realisations of the mask image based on P and L_R can be performed with an empirical procedure derived from the rigorous one described in the previous section, which works well for random fields of real values. The mask images, that have only binary values, can be

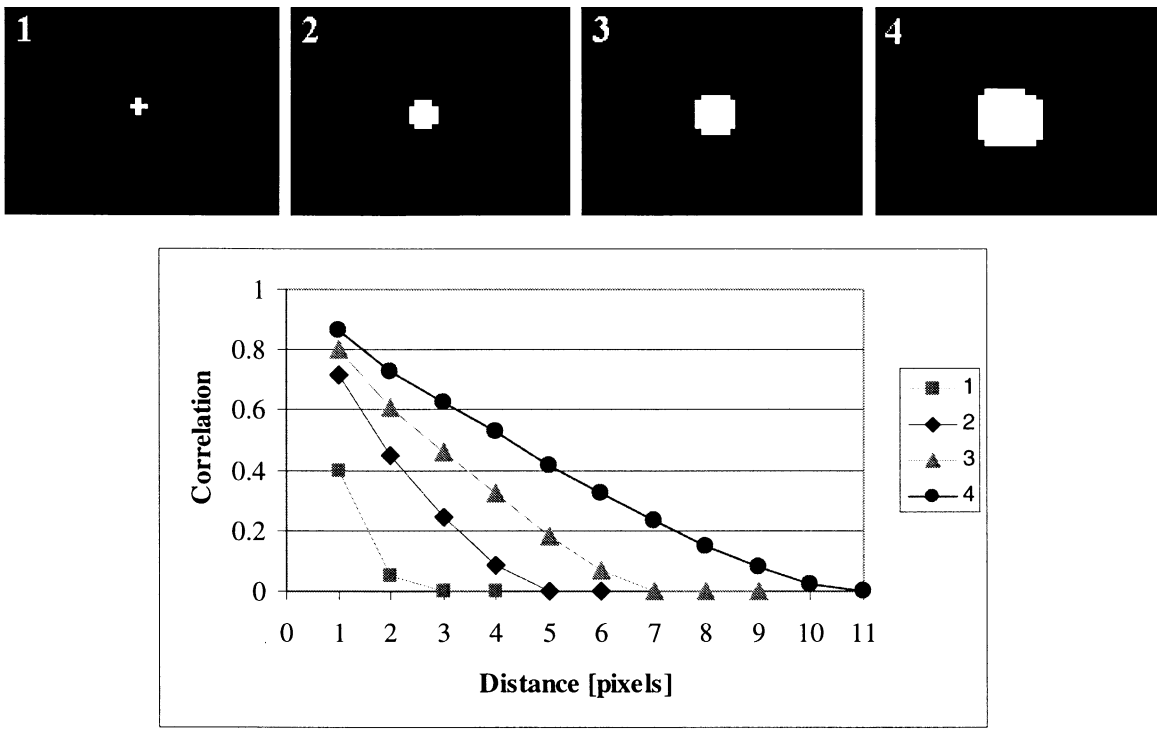

Fig. 2. EAFs computed for four different synthetic mask images (mask pixels are white). The correlation length can be chosen as suitable parameter to represent the level of mask aggregation.

derived by binarisation (i.e. forcing the real values to take binary values) of a field F of real values, whose correlation length is approximately L_R. The trick consists of choosing a MAF with correlation length of about L_R, and with a variance of the white noise $\sigma^2_{F\_W}$ that is much less than $\sigma^2_{F\_Corr}$. The binarisation is performed taking advantage of the known distribution of the generated field F. F is given by:

$$F = \mathrm{L} \cdot \mathrm{W},$$

where L is the lower triangular matrix of the Cholesky decomposition of C_{FF}. Since W is a normally distributed random field, F, which is a linear combination of W, is again normally distributed with known mean and variance. Therefore, a range of values of F can be chosen, which corresponds to a probability *P*. In this way, the procedure allows the random generation of mask images to be performed, with a given proportion of mask pixels *P* and a fixed level of mask aggregation. The characteristics of the generated images can be checked by computing their *P* and EAF.

An example of mask image simulation is illustrated in Fig. 3. A synthetic image was used as master image, i.e. as *R*. It has $P = 33.81\%$ and EAF with correlation $c = .33$ at the first lag and with zero correlation at the other lags. The generated mask image has a $P = 33.79\%$ and a very similar correlation structure, with $c = .26$ at first lag and zero otherwise. The level of aggregation can also be evaluated visually. It is important to keep in mind that with this procedure only the homogeneous and isotropic correlation structures of the mask images are addressed.

The choice of the input factor to be associated with the generation of mask images faces the same problem described for the stochastic error. In fact, assuming a fixed C_{FF}, the parameter *P* controls the generation of $l \times m$ binary values. An empirical way to treat this parameter is to use a random switch between two configurations as an input factor: In the first one, the mask image is generated and associated with the 2D field, while in the second one, the mask image is not considered. The sensitivity index associated with such an input factor measures the sensitivity of the model output to the switch, and hence it gives an indication of the sensitivity to the uncertainty represented by the mask effect.

6. Case study

UA and SA were performed on the output of a burned area detection model based on the Pathfinder AVHRR 8 km data set. The burned area of the whole African continent in the period 1982–1993 was considered in this work. The objective of the analysis was to identify, out of all uncertainties that affect input data and model parameters, the most influential ones, i.e. those that have the strongest influence on the output uncertainty.

The algorithm of Barbosa, Gregoire, and Cardoso Pereira (1999) was used in this work to extract burned areas from the NOAA/NASA Pathfinder AVHRR 8 km Land Data Set (James & Kalluri, 1994). This algorithm was originally developed for burned area extraction from AVHRR GAC 5 km data. It was employed to estimate burned areas for the whole African continent in the period 1981–1991 (Barbosa, Stroppiana, Gregoire, & Cardoso Pereira, 1999).

The algorithm employs three different types of thresholds: fixed, temporal, and automatic thresholds (see, for details, Barbosa, Gregoire, et al., 1999). It works pixelwise without considering the values of neighbourhood pixels. For a given week, a first selection is performed by a sequence of fixed thresholds, which aims to identify all potentially burned pixels. A more severe selection is obtained with the temporal thresholds, based on comparison of pixel values of week pairs in succession. The last type of threshold acts as a mask, preventing false fire detection. Two fixed

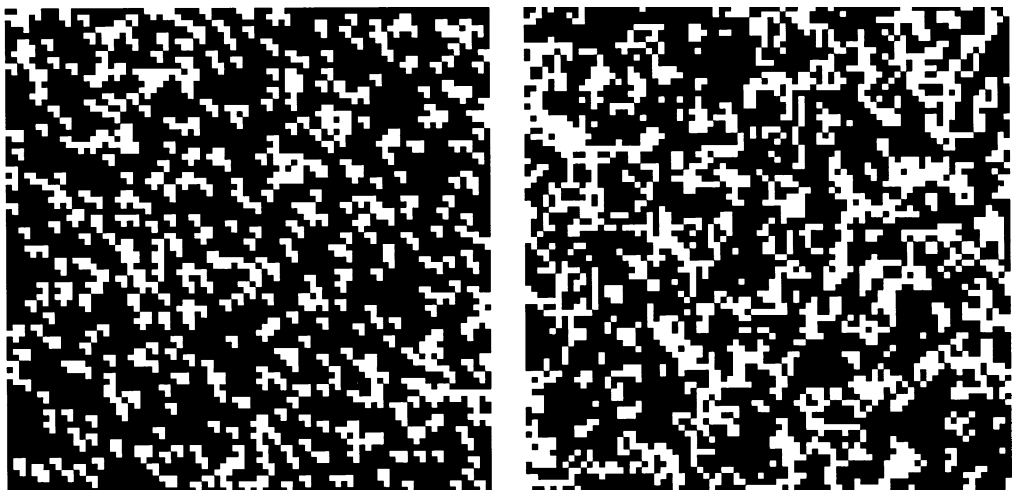

Fig. 3. Example of mask image simulation, with a synthetic master image (left side) and the corresponding generated mask image (right side).

thresholds were analysed in this work: the threshold on channel 2, expressed in percent, Ch2 < 12.5%, and that on channel 3, expressed in Kelvin, Ch3 > 312 K.

The Pathfinder AVHRR data set contains daily, global terrestrial data. Each daily data set contains 12 layers: channel 1 (Ch1, 0.58–0.68 μm) and channel 2 (Ch2, 0.73–1.10 μm) reflectances; channel 3 (Ch3, 3.55–3.93 μm), channel 4 (Ch4, 10.3–11.3 μm), and channel 5 (Ch5, 11.5–12.5 μm) brightness temperatures; CLAVR flag, i.e. the flag from the Clouds from AVHRR algorithm (Stowe, Davis, & McClain, 1999); scan angle; solar zenith angle; etc. A threshold on the CLAVR values is employed to mask the cloudy pixels. The uncertainty associated with this threshold was considered in the analysis.

Besides the uncertainty in model parameters (the Ch2 threshold, T2, the Ch3 threshold, T3, and the CLAVR threshold), the errors that affect the model input, i.e. the AVHRR Ch1, Ch2, and Ch3, were considered in the analysis.

6.1. Uncertainty in input data: AVHRR channels 1, 2, and 3

For AVHRR Ch1, Ch2, and Ch3, error model (3) was employed. In the following, the systematic and stochastic errors are described.

The Ch1 and Ch2 (hereafter denoted by Ch1/2) reflectances are strongly dependent on the variation of the geometrical conditions of data acquisition. The NOAA 7, 9, and 11 satellites, used to acquire the Pathfinder data set, were programmed to maintain a fixed time of Earth observation or Sun-synchronous operation. However, due to orbit degradation, the afternoon passes of the satellites were affected by a drift of 1–3 h in local overpass time (Price, 1991). This drift results in a systematic effect over the observed Ch1/2 reflectances, which affects the inter-annual data comparison for burned area detection. The burned area detection procedure is very vulnerable to this effect because it does not explicitly model the bidirectional reflectance (the reflectances are simply normalised with the cosine of the solar zenith angle), and it employs fixed thresholds for the whole period.

The systematic effect on Ch1/2 was evaluated through simulations with 6S (Second Simulation of the Satellite Signal in the Solar Spectrum) (see Vermote, Tanré, Deuzé, Herman, & Morcrette, 1998). 6S allows the simulation of the apparent reflectance at the top of atmosphere modelling both the bidirectional reflectance of the surface and the atmosphere (for details, see Vermote, Tanré, Deuze, Herman, & Morcrette, 1997). Statistics on the geometric configurations of acquisition of the Pathfinder data set were computed. In particular, for a set of 50 × 50 pixel windows evenly distributed over Africa, the temporal profiles of the solar zenith angle Z_{SUN}, the scan angle, and the relative azimuth angle were computed for the entire 11-year period. Five Z_{SUN} profiles of a window located in Zambia (Fig. 4) show the important variation in Z_{SUN} values between years. This variation becomes extreme in 1984 and the first 6 weeks of 1985, the latter part of the NOAA-9 data, acquired with very late satellite passes.

The computed profiles were input to 6S to simulate the corresponding profiles of the Ch1/2 reflectances. The bidirectional reflectance was modelled with the model proposed

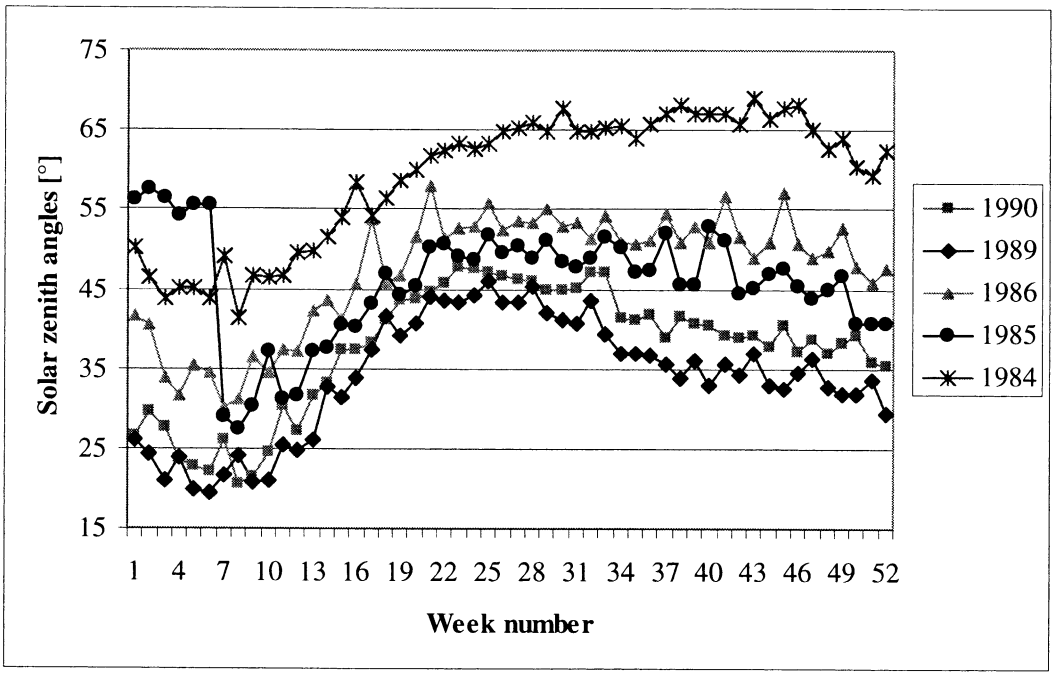

Fig. 4. AVHRR 8-km land data set. Annual solar zenith angle profiles of a 50 × 50 pixel window located in Zambia (approximate coordinates: $\varphi = 26°$, $\lambda = -15°$).

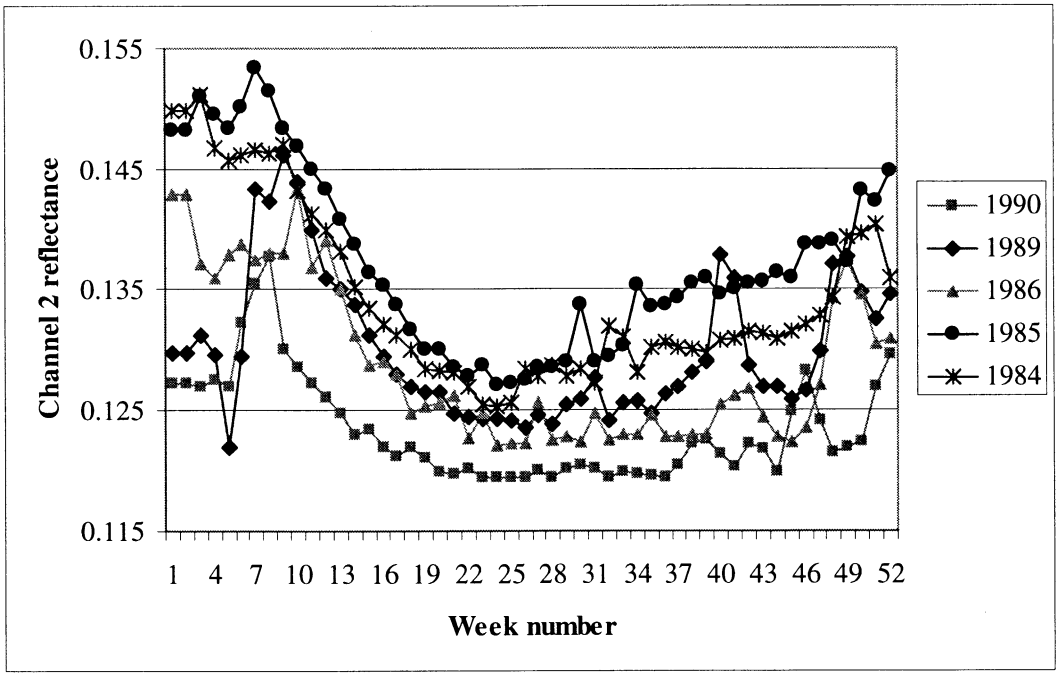

Fig. 5. AVHRR Ch2 reflectance profiles of savannah corresponding to the solar zenith angle profiles of Fig. 4. The reflectance values were simulated using 6S, adopting the model proposed by (Rahman et al., 1993) with the parameters $\rho_0 = 0.091$, $\Theta = -0.156$ and $k = 0.726$.

by Rahman et al. (1993), considering a savannah as cover type. The Ch2 profiles corresponding to the Z_{SUN} profiles of Fig. 4 are depicted in Fig. 5.

For each simulation scenario, that is for a given channel and a fixed window, the 11-year median profile was computed and afterwards subtracted from each annual profile. The resulting profiles, called difference profiles, were used to estimate the Ch1/2 biases. In a first approximation, the biases were assumed temporally constant. A more general pattern could be, however, introduced. The maximum amplitude of the difference profiles (i.e. the maximum bias) is proportionally dependent on the amplitude of the corresponding median profile. By analysing different scenarios, it was found that the maximum bias is about 7–10% of the median profile amplitude. For the MC simulation, the systematic errors on Ch1 and Ch2 were assumed to be uniformly distributed in the range [−7,7%] of the nominal reflectance values (see Table 1). Since in the considered cover type the simulated biases on Ch1 and Ch2 were highly correlated, only one input factor was chosen to drive the generation of the Ch1/2 biases. This result was extended to other cover types concerned with fires (e.g. Sahelian savannah, Miombo, etc.).

The stochastic error on Ch1/2 was estimated considering different pairs of 50×50 pixel windows over the Saharan desert. The desert was chosen because for Ch1/2, it can be considered a radiometrically stable target. From the considered pairs, acquired with a time interval of 7–14 days, the difference images were computed and used to assess the characteristics of the stochastic errors associated with Ch1/2. These errors include several components: radiometric instability of the sensor, the effect of atmospheric variations (in particular of water vapour and atmospheric aerosols), the effects of image registration, etc.

For both Ch1/2, the estimates of the error standard deviations σ_N obtained with the set of difference images

Table 1
Modelling of uncertainty in input data and model parameters

Input data and model parameters	Description of the associated uncertainty	Distributions
Channels 1 and 2	Systematic error (bias) temporally constant	U:[−0.07,0.07] of the nominal reflectance values
Channels 1 and 2	Stochastic error on reflectance values	N:[0,1.6%]
Channel 3	Systematic error (bias) spatially temporally constant	U:[−2,2 K]
Channel 3	Stochastic error on brightness temperatures	N:[0,2 K]
CLAVR threshold	Masks related to the partially cloudy (mixed) pixels	Fixed proportion of mask pixels P (variable over Africa)
Ch2 threshold	Uncertainty on threshold	U:[−1,1%]
Ch3 threshold	Uncertainty on threshold	U:[−2,2 K]

The uniform distribution is denoted by U:[range], while the normal distribution is denoted by N:[mean, standard deviation]

were quite similar (all the estimated σ_N are in the range 1.4–1.8%). The same cannot be said for the estimated correlation structure of the error field. For some difference images, the variance of the correlated part of the error $\sigma^2_{N\_Corr}$ is comparable to that of the white noise $\sigma_{N\_}\mathbf{w}^2$, and the correlation length L_N is about 10–15 pixels. An example is given in Fig. 1, where $\sigma^2_{N\_Corr}$ equals 34% of σ^2_N, and L_N is about 16 pixels. This large correlation length could be due to some trend in the analysed Ch1 values. For other difference images, the correlated part of the error plays a minor role. For instance, for some of them $\sigma^2_{N\_Corr}$ is less than 10% of σ^2_N. Therefore, in the MC simulation, the correlated part of stochastic errors on Ch1/2 was disregarded, assuming the error to be a white noise.

The stochastic error on Ch1 is highly correlated with the error on Ch2 (all the correlation coefficients calculated on pairs of Ch1 and Ch2 difference images were above .95). Furthermore, the errors on Ch1 and Ch2 have very similar σ^2_N. For this reason, in the MC simulation, the same error was applied on Ch1 and Ch2, i.e. the same input factor was used to drive the generation of realisations of Ch1/2 images. The input factor was a switch suitable to control the generation of a normally distributed error with zero mean and standard deviation of 1.6% (see Table 1). This error, estimated over the Saharan desert, was employed for the whole of Africa.

The above procedure could not be employed to assess the errors of Ch3. The reflected and emitted components of Ch3 radiation make the error analysis difficult. Furthermore, statistics based on difference images cannot be used because the target variations cannot be disregarded. Comprehensive estimates of the magnitude of errors associated with Ch3 brightness temperatures are not available, at least to the knowledge of authors. Therefore, assumptions on the error magnitude were made. A temporally and spatially constant bias, uniformly distributed in the range [−2,2 K], was considered. Furthermore, a stochastic error, spatially uncorrelated and normally distributed with zero mean and standard deviation of 2 K was used (see Table 1). As described below, the bias and the stochastic error on Ch3 have very low impact on the total burned area variance. For this reason, alternative assumptions on error scenarios were not considered in the analysis.

6.2. Uncertainty in model parameters: thresholds

T2 and T3 are the most important fixed thresholds of the model. They are intended to separate the potentially burned pixels from all others. The uncertainty was modelled with uniformly distributed errors in the range [−1,1%] and [−2,2 K] for T2 and T3, respectively.

The uncertainty associated with a third model parameter, the CLAVR threshold (TC), was considered in this work. The CLAVR values correspond to three pixel classes: clear, mixed, and cloudy pixels (Agbu & James, 1994). In the choice of TC, it was hypothesised that the following problem related to mixed pixels exists: Burned areas can be sometimes detected in mixed pixels; however, there is a possibility of confusing burned areas and certain types of cloud shadow. In this context, eliminating all mixed pixels can cause errors of omission in the burned area detection while accepting all of them can result in errors of commission (false detection). In this work, a TC value was chosen which accepts all clear and mixed pixels. However, this represented a subjective choice that was not supported by experimental evidence.

Therefore, an alternative value for TC, denoted by TC_A was considered: With TC_A, 33% of mixed pixels are rejected. The effect of choosing TC vs. TC_A was evaluated in the SA. The subjective decision TC vs. TC_A was represented by a switch between two alternative model versions: the nominal one with TC, and the other one with TC_A. This was practically obtained by generating mask images whose proportion of mask pixels P was evaluated through statistics on mixed pixels of the Pathfinder data set. For the main African land cover classes (the land cover map of the Maryland University, obtained from AVHRR GAC data, De Fries, Hansen, Townshend & Sohlberg, 1998, was used), the average proportions P_M of mixed pixels were computed. In the mask image generation, for each land cover class a value $P=P_M/3$ was used: 0.7% for desert; 8.0% for wooded grasslands; 12.9% for woodlands, etc. In a first analysis step (based on a portion of the entire considered area), the spatial aggregation of the masks was considered, assuming the same level of aggregation of the simulation example described in Section 5.3 (see Fig. 3). However, due to the low sensitivity index of the switch TC vs. TC_A (see the next section), it was verified that the mask spatial aggregation has a negligible effect on the SA results. Therefore, the spatial aggregation of masks was not considered in the MC simulation performed on the whole African continent.

Seven input factors were employed in the MC simulation (Table 1): two factors, systematic error and switch for stochastic error, for Ch1 and Ch2; two factors, systematic error and switch for stochastic error, for Ch3; one factor for T2; one factor for T3; and a switch between TC and TC_A.

Table 2
Results of SA based on the extended FAST: first-order indices and (nonnormalised) total order indices

Input factors	First-order indices [%]	Total order indices [%]
Bias on Ch1 and Ch2	34.2	37.2
Stochastic error on Ch1 and Ch2	6.8	8.1
Bias on Ch3	3.6	5.3
Stochastic error on Ch3	0.1	0.9
Switch TC vs. TC_A	4.6	9.0
Threshold channel 2	39.5	42.6
Threshold channel 3	6.4	9.4

6.3. Results

The MC simulation was performed on the whole African continent for the year 1990 using 2190 runs. The number of MC runs is discussed further in this section. The results of the SA are reported in Table 2. Two input factors drive most of the total burned area uncertainty: the threshold on Ch2 and the bias on Ch1 and Ch2.

In the model, T2 is intended to separate in a first approximation the potentially burned pixels from all others. Therefore, a low impact of its associated input factor was expected. Surprisingly, the associated sensitivity indices are high, the total order index S_{Ti} equals 42.6%, indicating that T2 does not behave as expected. This could be partially due to the difference between the AVHRR 8 km data set and the AVHRR 5 km data set used in Barbosa, Gregoire, et al. (1999). Nevertheless, this result clearly indicates that the modeller's attention has to be focused on the T2 value.

The bias on Ch1 and Ch2 has the second greatest effect on output uncertainty. This result gives an important hint to the modeller: An improvement of the precision of the model estimates requires the development of a suitable data preprocessing or a new modelling strategy in order to reduce the influence of systematic effects on Ch1/2 reflectances.

The low sensitivity index associated with the switch TC vs. TC_A, S_i equals 4.6%, indicates that the choice between TC and TC_A has little influence on the model output. The other input factors have also little influence on the output uncertainty. This means that further improvements of the model should not be concerned with their associated input data and model parameters. For instance, it is not wise to develop a preprocessing module to reduce the effect of stochastic error on Ch3 because its impact on the output is already negligible.

Table 3
Analysis of the precision (mean and standard deviation) of the total order sensitivity indices, calculated with five series of 1465 and 2190 runs, respectively

	FAST total order indices			
	1465 runs		2190 runs	
Input factors	Mean [%]	Standard deviation [%]	mean [%]	Standard deviation [%]
Bias on Ch1 and Ch2	46.3	8.0	45.4	3.6
Stochastic error on Ch1 and Ch2	13.7	3.0	9.5	1.7
Bias on Ch3	4.7	0.7	2.5	0.4
Stochastic error on Ch3	1.3	0.2	1.4	0.3
Switch TC vs. TC_A	5.1	0.4	5.5	2.3
Threshold channel 2	36.4	9.9	42.2	2.8
Threshold channel 3	3.5	0.9	3.8	0.3

The quality of the sensitivity estimates obtained through SA is related to the number of MC runs N_{MC}. In order to analyse the precision of the estimates reported in Table 2, two series of SA were performed on a 230×420 pixel window of the African continent. In particular, two series of SA with 1465 and 2190 runs, respectively, were performed five times, yielding a total of 10 estimates of the SA indices. The results of the two SA series, summarised by the means and the standard deviations of the estimated indices, are reported in Table 3. The precision obtained with 2190 runs is better than that obtained with 1465. A total of 2190 runs (i.e. about 300 runs for input factor) provided a precision that was considered sufficient for the objective of this study. However, this result cannot be generalised because the precision of the sensitivity estimates is greatly influenced by the structure of the model under analysis.

The above results were obtained through SA. Besides SA, the UA was performed. The 75% confidence limits on the total burned pixels are 63 456 and 152 752. It must, however, be noted that in this context, the confidence interval is overestimated because some sources of output uncertainty, like those due to model parameters, were artificially introduced in the MC simulation in order to perform the SA. Future developments of this work should include a more detailed UA, to be performed on the whole African continent and for the entire period 1982–1993.

7. Conclusions

In this paper, a general procedure to characterise the uncertainty associated with the output of RS models has been proposed. The procedure involves four main steps:

- the identification of all sources of uncertainty in the given model;
- uncertainty or error modelling;
- uncertainty propagation; and
- sensitivity analysis.

An error model for quantitative raster data, the most common RS input data type, has been extensively discussed and a rigorous procedure to characterise and simulate the associated errors has been proposed. An extension of the procedure has been discussed which allows a particular type of uncertainty in RS data, the mask effect due to cloud cover, to be taken into account in UA and SA. A numerical method for error propagation, the MC method, has been described. Since it treats models as black boxes, it represents a flexible tool for UA, which is generally applicable in the field of RS models.

Some possible applications of UA and SA have been described. UA and SA were used in the analysis of a RS model for burned area detection based on the Pathfinder AVHRR 8 km data set. The objective of the analysis was to evaluate the model behaviour, identifying the most impor-

tant sources of uncertainty. Both errors in input data and uncertainties in model parameters were considered. The errors associated with the input data, namely the AVHRR Ch1, Ch2, and Ch3, were decomposed in systematic and stochastic components. The error characteristics were derived either through statistics and simulations, or assuming given error levels. The uncertainty on model parameters was modelled either transforming threshold values in random variables, or adopting a random switch between two alternative versions of the model.

The results give important hints to understand the model behaviour. In order to improve the model, the attention should be focused on the two most influential input factors. The case study shows that UA and SA can be employed as effective tools in RS modelling. A future development of this work will be the UA of the extracted burned areas of the whole African continent in the period 1982–1993. The analysis will support a quantitative study of the evolution of the burned areas, focused on interannual comparison, analysis of trends, etc.

Acknowledgments

Data used in this study include data provided by the Distributed Active Archive Center at Goddard Space Flight Center, Greenbelt (USA). The software used to perform SA was kindly provided by Dr. Andrea Saltelli and Dr. Stefano Tarantola of the Institute for Systems, Informatics and Safety of the Joint Research Centre. The authors thank the Global Vegetation Monitoring Unit of the Joint Research Centre for the support provided during this work.

References

Agbu, P. A., & James, M. E., (1994). The NOAA/NASA Pathfinder AVHRR Land Data Set user's manual. Goddard Distributed Active Archive Center, NASA, Goddard Space Flight Center, Greenbelt, USA.

Barbosa, P. M., Gregoire, J. M., & Cardoso Pereira, J. M. (1999). An algorithm for extracting burned areas from time series of AVHRR GAC data applied at a continental scale. *Remote Sensing of Environment*, *69*, 253–263.

Barbosa, P. M., Stroppiana, D., Gregoire, J. M., & Cardoso Pereira, J. M. (1999). An assessment of vegetation fire in Africa (1981–1991): burned areas, burned biomass, and atmospheric emissions. *Global Biogeochemical Cycles*, *13* (4), 933–950.

Barzaghi, R., & Crippa, B. (1990). 3-D collocation filtering. In: A. Guen, & E. Baltsavias (Eds.), *Close-range photogrammetry meets machine vision*, *Proceedings SPIE*, 1395, 886–893. Washington.

Crosetto, M., & Tarantola, S. (2001). Uncertainty and sensitivity analysis: tools for GIS-based model implementation. *International Journal of Geographic Information Science* (in press).

Cukier, R. I., Fortuin, C. M., Schuler, K. E., Petschek, A. G., & Schaibly, J. H. (1973). Study of the sensitivity of coupled reaction systems to uncertainties in rate coefficients: Part I. Theory. *Journal of Chemical Physics*, *59* (8), 3873–3878.

De Fries, R. S., Hansen, M., Townshend, J. R. G., & Sohlberg, R. (1998). Global land cover classifications at 8 km spatial resolution: the use of training data derived from Landsat imagery in decision tree classifiers. *International Journal of Remote Sensing*, *19* (16), 3141–3168.

Goodchild, M. F., Guoqing, S., & Shiren, Y. (1992). Development and test of an error model for catagorical data. *International Journal of Geographic Information Systems*, *6*, 87–104.

Granshaw, S. I. (1980). Block adjustment methods in engineering photogrammetry. *Photogrammetric Record*, *10*, 181–207.

Heuvelink, G. B. M. (1998). *Error propagation in environmental modelling with GIS*. London: Taylor and Francis.

James, M. E., & Kalluri, S. N. V. (1994). The pathfinder data set: an improved coarse resolution data set for terrestrial monitoring. *International Journal of Remote Sensing*, *15* (17), 3347–3363.

Knudsen, P. (1987). Estimation and modelling of the local empirical covariance function using gravity and satellite altimeter data. *Bulletin Géodésique*, *61* (2), 145–160.

Mikhail, E. M. (1976). *Observations and least squares*. New York: Dun-Donelley.

Moritz, M. (1980). *Advanced physical geodesy*. Karlsruhe: Herbert Wichmann Verlag.

Pinty, B., Verstraete, M., & Dickinson, R. E. (1990). A physical model of the bidirectional reflectance of vegetation canopies: Part 2. Inversion and validation. *Journal of Geophysical Research*, *95*, 11767–11775.

Price, J. C. (1991). Timing of NOAA afternoon passes. *International Journal of Remote Sensing*, *12* (1), 193–198.

Rahman, H., Pinty, B., & Verstraete, M. (1993). Coupled surface–atmosphere reflectance (CSAR) model 2. Semiempirical surface model usable with NOAA Advanced Very High Resolution Radiometer data. *Journal of Geophysical Research*, *98*, 20791–20801.

Saltelli, A., Chan, K., & Scott, M. (Eds.). (2000). *Sensitivity analysis*. New York: Wiley.

Saltelli, A., Tarantola, S., & Chan, K. (1999). A quantitative model-independent method for global sensitivity analysis of model output. *Technometrics*, *41* (1), 39–56.

Sansò, F. (1986). Statistical methods in physical geodesy. In: H. Suenkel (Ed.), *Mathematical and numerical techniques in Physical Geodesy Lect Notes in Earth Sciences*, (pp. 49–156). Berlin: Springer.

Sobol', I. M. (1993). Sensitivity analysis for non-linear mathematical models. *Mathematical Modelling and Computational Experiment*, *1*, 407–414.

Stowe, L. L., Davis, P. A., & McClain, E. P. (1999). Scientific basis and initial evaluation of the CLAVR-1 global clear/cloud classification algorithm for the Advanced Very High Resolution Radiometer. *Journal of Atmospheric and Oceanic Technology*, *16*, 656–681.

Vermote, E., Tanré, D., Deuzé, J. L., Herman, M., & Morcrette, J. J. (1997). *Second simulation of the satellite signal in the solar spectrum (6S). 6S User's Guide Version 2*. Greenbelt, USA: NASA-GSFC.

Vermote, E., Tanré, D., Deuzé, J. L., Herman, M., & Morcrette, J. J. (1998). Second simulation of the satellite signal in the solar spectrum: an overview. *IEEE Transactions on Geoscience Remote Sensing*, *35* (3), 675–686.